ACS APPLIED MATERIALS & INTERFACES

Research Article

www.acsami.org

Fabrication of Au/Graphene-Wrapped ZnO-Nanoparticle-Assembled Hollow Spheres with Effective Photoinduced Charge Transfer for Photocatalysis

Nguyen Tri Khoa,[†] Soon Wook Kim,[†] Dae-Hwang Yoo,[†] Shinuk Cho,[†] Eui Jung Kim,[‡] and Sung Hong Hahn*,[†]

[†]Department of Physics and Energy Harvest−Storage Research Center and [‡]Department of Chemical Engineering, University of Ulsan, Ulsan 680-749, South Korea

Supporting Information

ABSTRACT: Heterostructures of gold-nanoparticle-decorated reduced-graphene-oxide (rGO)-wrapped ZnO hollow spheres (Au/rGO/ZnO) are synthesized using tetra-*n*-butylammonium bromide as a mediating agent. The structure of amorphous ZnO hollow spheres is found to be transformed from nanosheet- to nanoparticle-assembled hollow spheres (nPAHS) upon annealing at 500 °C. The ZnO nPAHS hybrids with Au/rGO are characterized using various techniques, including photoluminescence, steady-state absorbance, time-resolved photoluminescence, and photocatalysis. The charge-transfer time of ZnO nPAHS is found to be 87 ps, which is much shorter than that of a nanorod (128 ps), nanoparticle (150 ps), and nanowall (990 ps) due to its unique structure. The Au/rGO/ZnO hybrid shows a higher charge-transfer efficiency of 68.0% in comparison with rGO/ZnO (40.3%) and previously reported ZnO hybrids. The photocatalytic activities of the samples are evaluated by photodegrading methylene blue under black-light irradiation. The Au/rGO/ZnO exhibits excellent photocatalytic efficiency due to reduced electron−hole recombination, fast electron-transfer rate, and high charge-transfer efficiency.

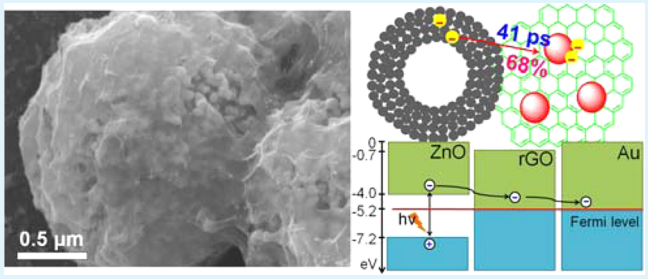

KEYWORDS: *graphene oxide, zinc oxide, gold nanoparticle, hierarchical aggregate, photoinduced reactivity, charge transfer*

INTRODUCTION

In recent years, heterostructural photocatalysts have greatly attracted attention in the photodegradation of organic pollutants, such as methylene blue, methyl orange, rhodamine, and phenol.[1−6] The principle of photocatalytic cells is based on the absorption of irradiated photons to create electron−hole pairs, which are separated and diffused across interfaces to react with adsorbed substances on the surface. The excited electron−hole pairs can recombine at the valence band edge or can be captured at trap sites (defects, vacancies).[7] Therefore, the enhancement of photoinduced charge transfer is crucial to improve the photocatalytic performance. There are several ways to improve charge transfer in a semiconductor. For example, metal nanoparticle, metal oxide, or carbon material decorated on the semiconductor surface facilitates electron transfer from the semiconductor to the metal via Schottky contact, serves as the cocatalyst material, or easily separates electrons from semiconductor surface, respectively.[8−12] Semiconductor photocatalysts, including TiO_2, ZnO, CdS, and ZnS, have been known as excellent materials for the photoinduced redox reaction due to their specific electronic structure (the filled valence band and empty conduction band) and have been used for the degradation of many hazardous compounds in water and air.[13] In particular, ZnO, a wide band gap semiconductor, has been widely researched as a photocatalyst in sustainable solar energy harvesting areas due to its abundant morphologies, easy synthesis, low cost, and nontoxicity.[14] Graphene, a two-dimensional honeycomb structure, has been known as an excellent material for improving the optoelectrical and electrochemical activities of hybrid materials.[15−18] Recently, reduced graphene oxide (rGO) based composite photocatalysts have gained increasing attention because they improve the charge transfer at the interface and have good adsorption capabilities for organic pollutants on their surfaces. Xu's research group has claimed that a graphene-based nanocomposite holds a great potential in the development of multifunctional photocatalytic performance.[19−27] This group reported that the enhancement of the photocatalytic activity of graphene−semiconductor results from the strengthened interfacial contact and optimized interfacial composition. Su and co-workers have fabricated rGO/ZnO hollow spheres to investigate the suppression of charge-carrier recombination for enhancing photocurrent and photocatalytic activities.[28] However, to the best of our knowledge, no studies have been reported on the photoinduced properties of Au/rGO/ZnO

Received: October 16, 2014
Accepted: January 28, 2015
Published: January 28, 2015

DOI: 10.1021/acsami.5b00152
ACS Appl. Mater. Interfaces 2015, 7, 3524−3531

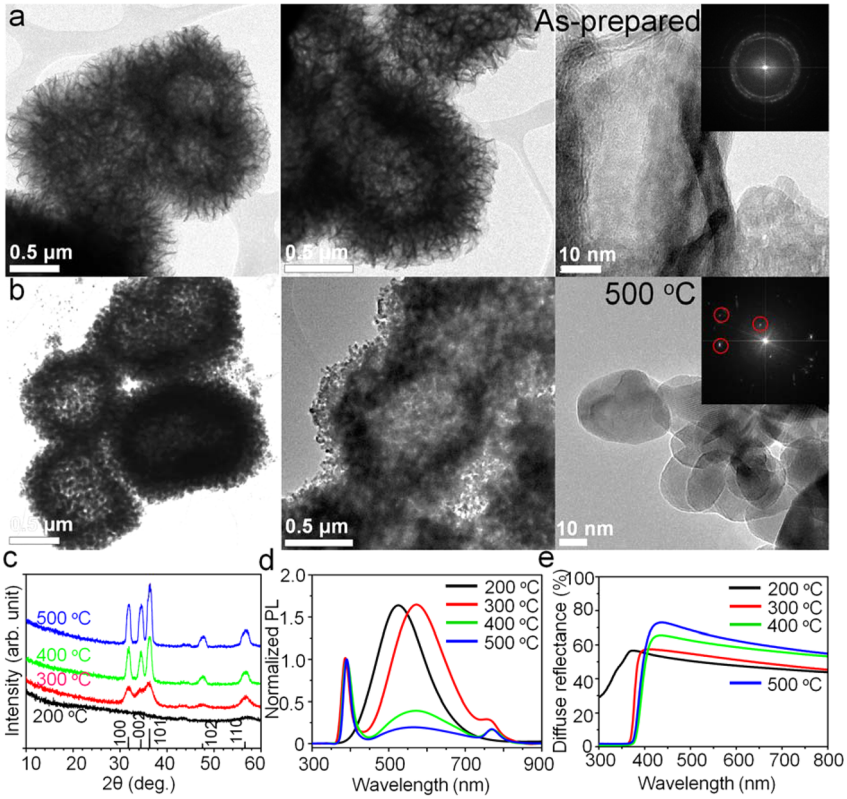

Figure 1. TEM, HR-TEM, and SAED images of as-prepared (a) and 500 °C-annealed (b) ZnO hollow hierarchical structure. XRD patterns (c), normalized PL spectra (d), and diffuse reflectance spectra (e) of ZnO annealed at various temperatures.

hybrid with ZnO hollow hierarchical structure for effective photoinduced charge transfer at the interface.

In this work, we synthesized a gold-nanoparticle-decorated rGO-wrapped ZnO hollow hierarchical heterostructure (Au/rGO/ZnO). Upon annealing at 500 °C, the ZnO structure is transformed from nanosheet-assembled (as-prepared ZnO) to nanoparticle-assembled hollow spheres (nPAHS). The charge-carrier lifetime of ZnO is much reduced when wrapped by rGO and much more reduced when wrapped by Au/rGO. This phenomenon demonstrates that wrapping Au/rGO on ZnO greatly improves the photoinduced charge-transfer efficiency and electron-transfer rate, resulting in the enhanced photocatalytic activities of the hybrid.

EXPERIMENTAL SECTION

Synthesis of ZnO Hollow Spheres. Zinc acetate dihydrate [$Zn(CH_3COO)_2{\cdot}2H_2O$] was dissolved in 100 mL of water in a 500 mL jar and stirred for 5 min, and then 0.1 mmol of trisodium citrate ($Na_3C_6H_5O_7$) was added to the precursor solution and the mixture was continuously stirred for 5 min. Subsequently, 1 mmol of hexamethylenetetramine [$(CH_2)_6N_4$] was introduced and the mixture stirred for 5 min. A glass substrate was located at the bottom of the jar to collect the precipitates. After a stopper was put on the jar, the solution was refluxed at 95 °C for 180 min. The as-prepared ZnO coated on glass substrate was cleaned by rinsing with ethanol, and then it was annealed at 500 °C for 60 min for further study.

Synthesis of Hybrid AuNPs/rGO/ZnO. Graphene oxide (GO) was synthesized using a modified Hummers method and reduced using hydrazine monohydrate 98% ($C_2H_4{\cdot}H_2O$).[29] To obtain rGO, 4 mL of aqueous GO (0.3 g/L) was mixed with 16 mL of ethanol and the mixture was ultrasonicated for 15 min. Hydrazine (0.4 mL) was then added and the mixture ultrasonicated for 60 min. To fabricate Au/rGO/ZnO hybrids, a mixture of 0.1 mL of 10 mM hydrogen tetrachloroaurate(III) ($HAuCl_4{\cdot}4H_2O$) and 0.9 mL of 20 mM tetra-*n*-butylammonium bromide (TBAB, $C_{16}H_{36}Br^-N^+$) was added to the as-prepared rGO solution and this mixture was ultrasonicated for 120 min (in the case of fabricating rGO/ZnO, only 0.9 mL of 20 mM TBAB was used). Subsequently, the resulting Au/rGO aqueous solution was added to 10 mL of ZnO (1 mg/mL) in ethanol and the mixture was ultrasonicated for 60 min to wrap Au/rGO nanosheets onto ZnO. The final suspension was washed with ethanol three times and then dispersed in 10 mL of water:ethanol (1:1 v/v) for spraying on a 2 × 2 cm^2 quartz substrate, which was mildly annealed at 150 °C for 30 min for further characterizations.

Characterization. Morphological properties of the samples were studied using field emission electron microscopy (FESEM) with a 10 kV operating voltage, transmission electron microscopy (TEM) with an electron gun of 200 keV, and atomic force microscopy (AFM) with an RTESP probe in a tapping mode. X-ray diffraction (XRD) with Cu Kα radiation was used to analyze the crystalline ZnO. X-ray photoelectron spectroscopy (XPS, Thermo Fisher, K-alpha) with 200 eV beam energy trained on a 400 μm spot size was employed to investigate chemical bonding. Nitrogen adsorption−desorption isotherms and Brunauer−Emmett−Teller (BET) surface areas were recorded on an accelerated surface area and porosimetry system (ASAP 2420 V2.09) at 77 K. The samples were degassed at 125 °C for 12 h before nitrogen adsorption measurement. The optical properties were analyzed using a UV−vis spectrophotometer (HP8453) with a 190−1100 nm wavelength and 1 nm slit width and a photoluminescence spectrometer on a He−Cd laser (IK3301R-G, Kimmon Koha) at room temperature with a wavelength of 325 nm and output power of 30 mW. The time-resolved photoluminescence spectra were taken at room temperature on a mode-locked femtosecond pulsed Ti:sapphire laser (Coherent, Chameleon Ultra II) at an excitation wavelength of 266 nm and output power of 0.2 mW. A streak camera (Hamamatsu, C7700-01) was used to measure the decay profile.

Photocatalytic Measurement. The as-prepared samples were dispersed in 10 mL of water:ethanol (1:1 v/v) for spray pyrolysis on a 2 × 2 cm^2 quartz substrate, which was then mildly annealed at 150 °C for 30 min. The sprayed samples on 2 × 2 cm^2 quartz substrate were

DOI: 10.1021/acsami.5b00152
ACS Appl. Mater. Interfaces 2015, 7, 3524−3531

used to evaluate the photocatalytic activity. The samples were immersed in 10 mL of 10 μM methylene blue ($C_{16}H_{18}N_3SCl{\cdot}3H_2O$) in water irradiated by five surrounding 20 W black-light (UVA) lamps (wavelength range 315−400 nm). The photocatalytic performance was analyzed by measuring the absorbance of the methylene blue solution at λ = 665 nm using a UV−vis spectrophotometer (HP8453) every 30 min for 150 min.

RESULTS AND DISCUSSION

Figure 1 shows the annealing-temperature-dependent morphological, crystalline, and optical properties of the ZnO hollow hierarchical assembly. TEM and HR-TEM images in Figure 1a confirm the hollow structure of the as-prepared ZnO, which is formed from the assembly of nanosheets around a hollow sphere. The selected area electron diffraction (SAED) image shows the amorphous structure of the as-prepared ZnO. The transformation of morphology from nanosheet- to nanoparticle-assembled hollow spheres (nPAHS) after annealing at 500 °C is shown in Figure 1b. The incorporation of oxygen from the air into the defects in the ZnO crystal during the annealing process induces the transformation of the morphology, the improvement of the crystallinity (SAED image), and the change of the optical properties of the ZnO hierarchical structure. The TEM images of the ZnO nPAHS in Figure S1 (Supporting Information) are additional evidence for the hollow sphere structure. XRD results in Figure 1c show that the crystallinity of the ZnO is improved with annealing from 200 to 500 °C. No peaks appear at 200 °C, indicating that the as-prepared ZnO is amorphous, which may result from the adsorption of citrate anions onto the ZnO surface. Peaks are observed at 300 °C, implying that crystals are formed and the adsorbed citrate anions on ZnO are thermally decomposed.[30] As the temperature is further increased up to 500 °C, the crystallinity of the ZnO is improved with increasing temperature, and the ZnO structure is transformed from assembled nanosheets to nanoparticles. The diffraction pattern of ZnO nPAHS is consistent with the wurtzite structure (JCPDS No. 36-1451; a = 3.241 96 Å and c = 5.211 11 Å). The photoluminescence (PL) of the annealed ZnO hollow spheres is illustrated in Figure 1d. The PL emission peak of the 300 °C-annealed ZnO is red-shifted in comparison with 200 °C-annealed ZnO. This phenomenon results from the modification of defects such as oxygen and zinc vacancies, interstitials, and antisites. The green emission of the 200 °C-annealed ZnO is typically associated with zinc vacancies and oxygen vacancies.[31] At an annealing temperature of 300 °C, the green band emission of ZnO is shifted to the yellow band due to the decreased concentration of zinc vacancies and the moderate concentration of oxygen vacancies.[32] The 500 °C-annealed ZnO is found to have the fewest defects compared to the other samples. This result confirms the removal of both zinc and oxygen vacancy defects to produce high-purity, high-crystalline ZnO nPAHS. The diffuse reflectance results in Figure 1e show that the optical absorbance property of ZnO depends strongly on annealing temperature. The red-shift of the absorbance edge and the decrease of absorbance in the visible range with increasing annealing temperature are ascribed to the enhanced ZnO crystallinity and the improved transparence properties of nanoparticles in comparison with nanosheets assembled into the hollow sphere structure. Due to its high crystallinity, high purity, and excellent optical properties, the 500 °C-annealed ZnO (nPAHS structure) is selected to study the effect of rGO and Au/rGO decoration on the photoinduced charge transfer and recombination at the ZnO interface.

The growth mechanism of the ZnO hollow structure was reported in our previous work.[33] With the assistance of trisodium citrate (Na_3-citrate), the hydroxyl and carboxyl groups in citrate ions cap Zn^{2+} precursors and direct the growth of the ZnO structure. At 95 °C under reflux, hexamethylenetetramine reacts with water to produce formaldehyde (HCHO) gas as follows:[33]

$$(CH_2)_6N_4 + 10H_2O \rightarrow 6HCHO(g) + 4NH_4^+ + 4OH^-$$

The Zn^{2+} precursor capped by the citrate ion covers the HCHO gas template to form a seed-layer-decorated hollow sphere (Figure 2a). Zn^{2+} and OH^- ions remaining in the reflux

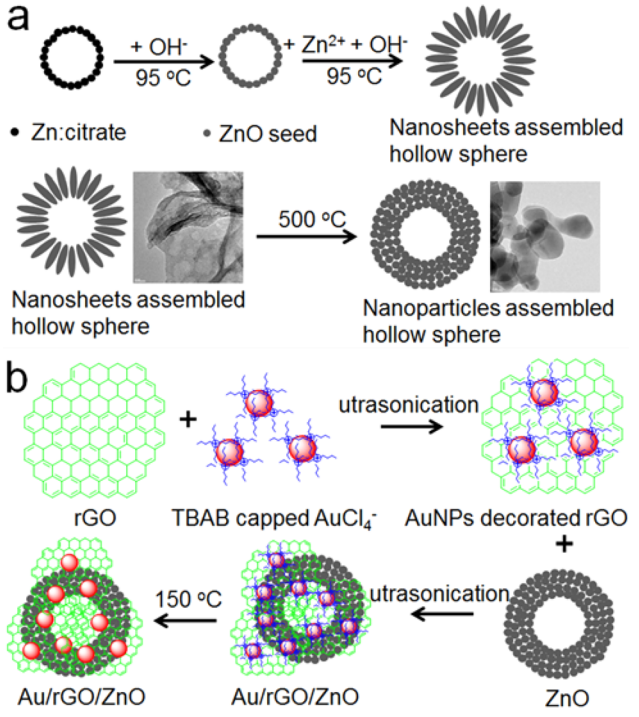

Figure 2. Schematic illustration of the synthesized ZnO hollow hierarchical structure (a) and the synthesis of Au/rGO/ZnO hybrid (b).

solution are consumed as ZnO hollow spheres continue to grow. The Na_3-citrate works as an inhibitor of [001] growth and facilitates the growth in the [100] direction to form the nanosheet-assembled hollow structure.[34] The resulting product was annealed at 500 °C to remove the citrate ion and improve the crystalline structure. As a result, the pure ZnO nPAHS was obtained, which possesses better optical properties than other samples.

A mechanism for the synthesis of Au/rGO/ZnO is schematically illustrated in Figure 2b. The rGO (obtained by reducing GO suspension with hydrazine monohydrate) is highly reduced, as shown in the XPS data (Figure S2, Supporting Information). The peaks for oxygen functional groups such as hydroxyl (C−OH), carbonyl (C═O), and carboxylic (O−C═O) are not observed in the XPS spectra of rGO. The TBAB (a cationic polymer) capped $AuCl_4^-$ is adsorbed on the negatively charged rGO plane under sonication to obtain Au/rGO hybrid. The AuNPs well-decorated onto rGO are revealed in AFM image in Figure S3

DOI: 10.1021/acsami.5b00152
ACS Appl. Mater. Interfaces 2015, 7, 3524−3531

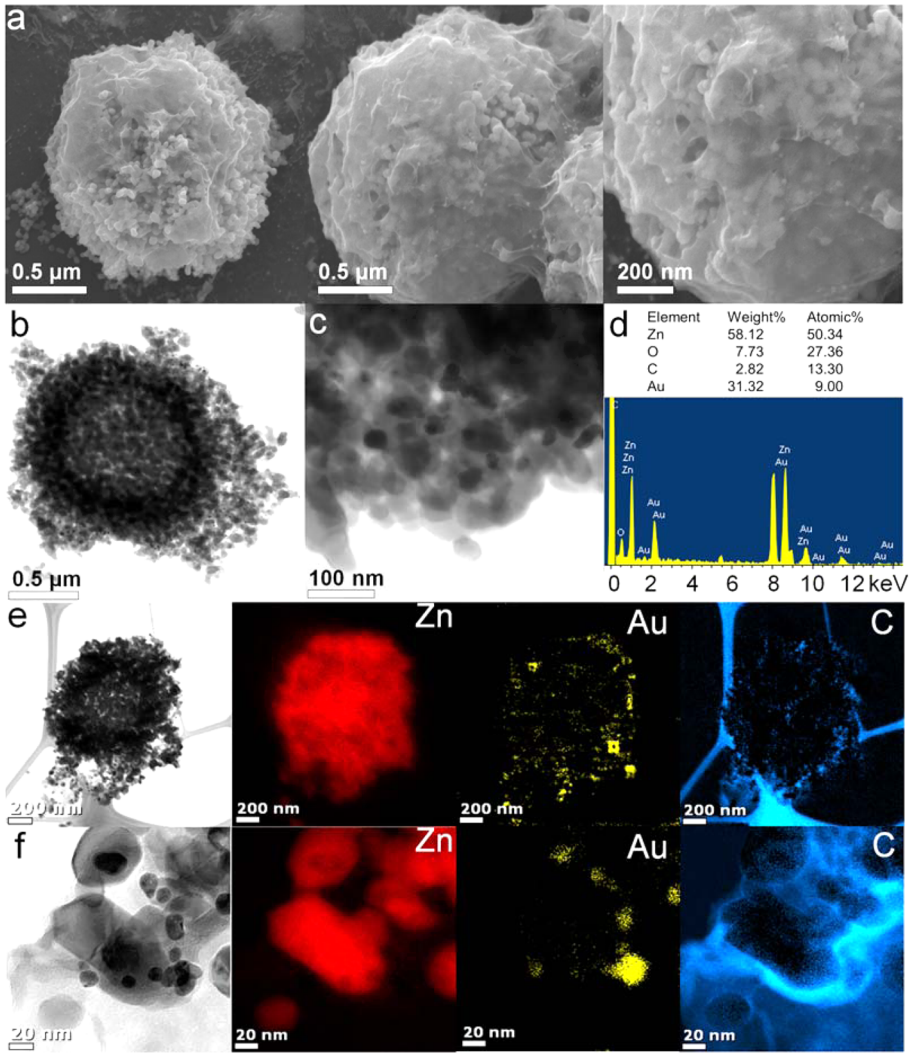

Figure 3. SEM (a), BF-STEM (b, c), EDX (d), BF-STEM and EELS chemical mapping (e), and high resolution BF-STEM and EELS chemical mapping (f) results of the Au/rGO-wrapped ZnO hollow hierarchical structure.

(Supporting Information). AuNPs are found to be about 10−20 nm in diameter, which are mostly located at the edge of rGO monolayer. The TBAB ligand in solution also plays an important role as a mediating material to wrap rGO onto ZnO and prevents the aggregation of the rGO sheets. The TBAB free ligand is also decorated on the ZnO hollow sphere to easily cover rGO under ultrasonication. After wrapping Au/rGO onto the ZnO interface, the TBAB can be removed from the Au/rGO/ZnO hybrid by mild annealing at 150 °C after the thermal spray-coating process.

Figure 3 shows the SEM, bright-field scanning TEM (BF-STEM), energy-dispersive X-ray spectroscopy (EDX), and electron energy loss spectroscopy (EELS) chemical mapping results of the Au/rGO-wrapped ZnO nPAHS structure. SEM images in Figure 3a clearly reveal that Au/rGO covers the entire ZnO nPAHS surface, which confirms the excellent adsorption of rGO on ZnO through the mediation of TBAB. For detailed analysis, BF-STEM (Figure 3b,c), EDX (Figure 3d), and EELS chemical mapping (Figure 3e,f) measurements are performed. The EDX measurement is taken at the ZnO hollow sphere edge to confirm the presence of rGO and Au at the ZnO interface. As shown in Figure 3d, the atomic content of Au and C is 9.0% and 13.3% in Au/rGO/ZnO composite, respectively. By taking EELS chemical mapping from a large-scale BF-STEM in Figure 3e, Au and C elements mostly exist at the edge of ZnO nPAHS, which shows the good decoration of Au and rGO on ZnO. Furthermore, high-resolution BF-STEM and EELS chemical mapping in Figure 3f are taken to investigate the morphological properties at the Au/rGO−ZnO interface. ZnO nanoparticles of about 50 nm in diameter are assembled to form a ZnO nPAHS structure of about 1.6 μm in size (Figure 3e,f); Au nanoparticles of about 10−20 nm in diameter are randomly distributed on the Au/rGO−ZnO nPAHS interface; and the excellent adsorption and covering of Au/rGO on the ZnO surface are also confirmed.

Figure 4 shows the UV−vis and PL spectra of ZnO nPAHS structures and their hybrids with rGO and Au/rGO. In the UV−vis spectra (Figure 4a), the absorbance peak of graphene appears at 265 nm and the plasmonic band of AuNPs from 500 to 630 nm, confirming the presence of rGO and AuNPs in the composite. The improved absorbance of Au/rGO/ZnO in comparison with rGO/ZnO could be due to the plasmonic light trapping effect of AuNPs.[35] When an incoming photon hits the AuNPs, the photon is trapped or scattered in many directions at the interface, enhancing the light absorption ability of the hybrid. As shown in the PL spectra (Figure 4b), the Au/

DOI: 10.1021/acsami.5b00152
ACS Appl. Mater. Interfaces 2015, 7, 3524−3531

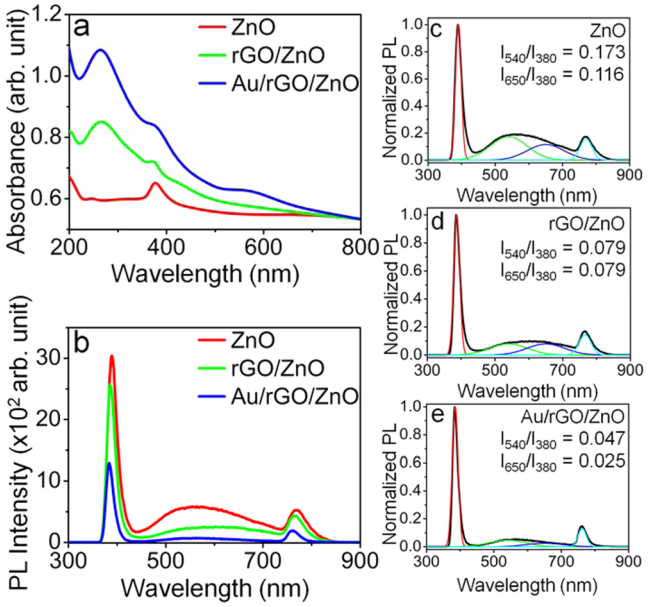

Figure 4. UV–vis (a) and PL spectra (b) of ZnO, rGO/ZnO, and Au/rGO/ZnO nPAHS. The normalized PL emission of ZnO (c), rGO/ZnO (d), and Au/rGO/ZnO (e) as four Gaussian-resolved peaks at 380, 540, 650, and 760 nm.

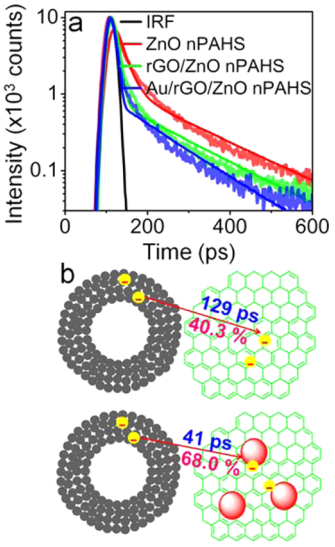

Figure 5. Time-resolved PL decay profile of ZnO, rGO/ZnO, and Au/rGO/ZnO nPAHS (a). The system instrument response function (IRF) is used as the reference. An illustration of electron transfer at the ZnO interface (b).

rGO/ZnO has the lowest emission intensity of the band gap peak (380 nm) and visible emission band. The normalized PL spectra (Figure 4c–e) are decomposed into four Gaussian emissions: band gap peak (380 nm) and deep-level point defects at 540 and 650 nm; the emission in the near-infrared region (760 nm) is considered as the second-order band gap peak. The decrease of the PL emission intensity in the case of wrapping rGO and Au/rGO on ZnO implies that electron transfer from the ZnO conduction band to the interface is facilitated. The generated electron in ZnO transfers to the rGO (lower energy state), which takes place faster than its recombination with a hole in ZnO. This effect is improved with the introduction of AuNPs in the composite, thus facilitating electron transport at the interface and quenching the recombination of electron–hole pairs. The emission ratios of defects/band gap are found to be decreased as ZnO is wrapped with rGO and Au/rGO, being 0.173, 0.079, and 0.029 (I_{540}/I_{380}) and 0.116, 0.079, and 0.025 (I_{650}/I_{380}) for ZnO, rGO/ZnO, and Au/rGO/ZnO, respectively. This result shows that electron transfer from the defect state to the interface is more facilitated than from the conduction band. The separated electron in the conduction band could be nonradiatively transited to surface defects such as oxygen vacancies and zinc interstitials (donor levels). With the strengthened interfacial contact between Au/rGO and ZnO, an electron could be facilitated to transfer from surface defects in ZnO to the Au/rGO layer. Thus, the surface defects of ZnO are expected to act as an active site for the interfacial charge transfer.

Figure 5 shows the time-resolved PL decay profile of the samples to evaluate the photoinduced charge transfer from the ZnO conduction band to the Au/rGO interface. As shown in Figure 4b–e, the defect emission of the ZnO nPAHS structure is so much weaker than that of the band gap/exciton. This leads to a low signal-to-noise ratio in measuring the time-resolved PL decay profile of the defect state using the Ti:sapphire laser (excitation wavelength of 266 nm and output power of 0.2 mW). Therefore, we use the result of the time-resolved PL of the band gap/exciton to exhibit the improving charge transfer at the ZnO–Au/rGO interface. The monitored peak in the time-resolved PL is the band gap peak (about 380 nm), as shown in Figure S4 (Supporting Information). From the double exponential fitting, the charge-carrier lifetimes ($\langle\tau\rangle$), charge-transfer lifetimes (τ_{CT}), and charge-transfer efficiency (η) are determined (Table 1). The fast component (τ_1) originates from the free exciton states, while the slow component (τ_2) is ascribed to the bound exciton states.[36] From the fitting data, both components τ_1 and τ_2 become shorter after wrapping ZnO with rGO and Au/rGO, which leads to a decrease in charge-carrier lifetime (τ_{ZnO} = 87 ps, $\tau_{rGO/ZnO}$ = 52 ps, and $\tau_{Au/rGO/ZnO}$ = 28 ps). From the relation $\tau_{CT} = (\tau_{Semi}\tau_{Hybrid})/(\tau_{Semi} - \tau_{Hybrid})$,[36,37] the charge-transfer time is faster in the presence of AuNPs, which is decreased from 129 ps for rGO/ZnO to 41 ps for Au/rGO/ZnO. The Au/rGO/ZnO with a faster charge-transfer time exhibits excellent charge-transfer efficiency compared with rGO/ZnO. The photoinduced charge-transfer efficiency is determined as η = 40.3% for rGO/ZnO and η = 68.0% for Au/rGO/ZnO. According to previous works, the charge-transfer efficiency was η = 20% for Au–ZnO nanoparticle hybrid (τ_{ZnO}= 150 ps, τ_{Hybrid} = 120 ps),[36] η = 31.3% for rGO/ZnO nanorod hybrid (τ_{ZnO} = 128 ps, τ_{Hybrid} = 88 ps),[38] and η = 53.6% for CdS/ZnO nanowall (τ_{ZnO} = 990 ps, τ_{Hybrid} = 460 ps).[39] Therefore, Au/rGO/ZnO nPAHS (η = 68.0% and τ_{CT} = 41 ps) synthesized in this work exhibits the better photoinduced charge-transfer efficiency and faster electron transport among ZnO hybrids reported so far.

The photocatalytic performance of the prepared ZnO hydrids is evaluated by measuring the photodegradation of methylene blue (MB) under black-light irradiation. As shown in Figure 6, the MB photodegradation efficiency of ZnO nPAHS is found to be 56%, increasing to 64% and 70% after being wrapped by rGO and Au/rGO, respectively. Novel, highly crystalline ZnO nPAHS shows much better photodegradation efficiency than P25 (41%). Good wrapping of Au/rGO onto ZnO, effective photoinduced electron transport, and excellent adsorption of negatively charged rGO onto MB account for the

DOI: 10.1021/acsami.5b00152
ACS Appl. Mater. Interfaces 2015, 7, 3524–3531

Table 1. Kinetic Parameters of the PL Emission Decay of ZnO Nanoparticle-Assembled Hollow Spheres and Their Hybrids with rGO and Au/rGO[a]

	a_1, %	τ_1, ps	a_2, %	τ_2, ps	$\langle\tau\rangle$, ps	τ_{CT}, ps	η, %
ZnO	91.8	20.2	8.2	174.4	87.1		
rGO/ZnO	98.3	6.6	1.7	160.1	52.0	129.0	40.3
Au/rGO/ZnO	99.5	2.6	0.5	129.2	27.9	41.0	68.0

[a]The double exponential profiles were fitted using the equation $I(t) = a_1 \exp(-t/\tau_1) + a_2 \exp(-t/\tau_2)$. The charge-carrier lifetime: $\langle\tau\rangle = (a_1\tau_1^2 + a_2\tau_2^2)/(a_1\tau_1 + a_2\tau_2)$. The charge-transfer lifetime: $\tau_{CT} = (\tau_{Semi}\tau_{Hybrid})/(\tau_{Semi} - \tau_{Hybrid})$. The charge-transfer efficiency: $\eta = \tau_{Hybrid}/\tau_{CT}$.[36,37]

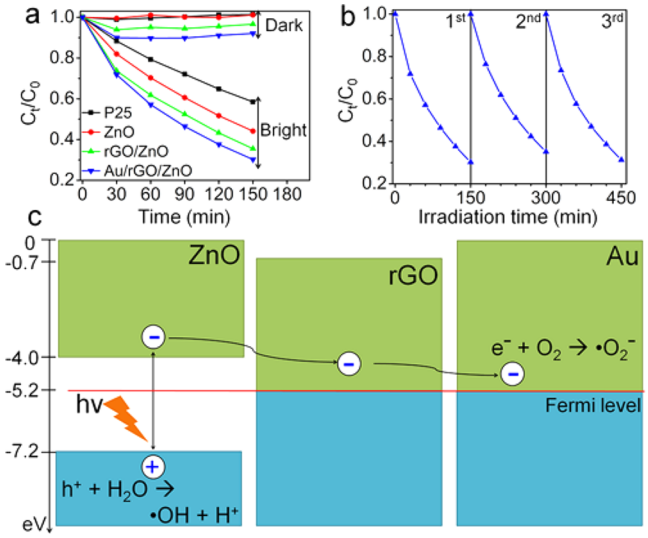

Figure 6. Photocatalytic performance of the ZnO samples compared with P25 (a) and repetitive photocatalytic test results of Au/rGO/ZnO (b). An illustration of the photocatalytic activities in Au/rGO/ZnO (c).

improved photocatalytic performance of rGO/ZnO. To examine the adsorption ability toward MB, the specific surface areas of ZnO, rGO/ZnO, and Au/rGO/ZnO have been determined from nitrogen adsorption−desorption isotherms and the BET surface areas shown in Figure S5 (Supporting Information). The BET surface area of ZnO, rGO/ZnO, and Au/rGO/ZnO is found to be 12.7, 17.9, and 28.9 m^2/g, respectively. Thus, the best photocatalytic performance of Au/rGO/ZnO results from both effective photoinduced charge transfer and excellent adsorption ability toward MB. Furthermore, the Au/rGO/ZnO shows an excellent photocatalytic activity for three cycles by consecutively photodegrading 70%, 65%, and 69% of MB, as shown in Figure 6b. This result demonstrates a stable photocatalysis and a strong adsorption of Au/rGO onto ZnO surface.

A mechanism for the photocatalytic acitivity of Au/rGO/ZnO is illustrated in Figure 6c. Typically, under UV-light irradiation, electron−hole pairs are generated in the photoactive ZnO. The work function of ZnO (5.2−5.3 eV) and AuNPs (5.1 eV) is different from that of rGO (4.5 eV), so photoexcited electrons transfer readily from ZnO to rGO and from rGO to AuNPs.[40−43] The Au/rGO layer has excellent adsorption properties (highest BET surface area value). Thus, photoexcited electrons trapped on Au/rGO can rapidly react with oxygen to form superoxide radicals ($O_2^{\bullet-}$) or hydroperoxide radicals for degrading organic pollutants. The remaining photoinduced holes can oxidize water or OH^- to produce a hydroxyl radical ($OH^{\bullet}$) that is able to oxide organic pollutants. An effective photoinduced electron transfer at the interface leads to an enhanced photocatalytic activity.

CONCLUSION

We have successfully synthesized the novel structures of ZnO nPAHS and Au/rGO/ZnO hybrid. Excellent covering of Au/rGO on ZnO in the hybrid results from the good adsorption properties of rGO through the mediation of cationic TBAB polymer. The Au/rGO/ZnO exhibits facilitated electron transfer across the Au/rGO−ZnO interface, fast and effective photoinduced charge transfer (τ_{CT} = 41 ps and η = 68%) resulting from good decoration of Au/rGO onto ZnO, plasmonic absorption enhancement, and strong perturbation of photon-excited electrons. As a result, with the excellent photoinduced separation and diffusion of electron−hole pairs, the Au/rGO/ZnO exhibits remarkable photocatalytic activity compared with ZnO and rGO/ZnO hybrid.

ASSOCIATED CONTENT

Supporting Information

TEM images of Au/rGO/ZnO, XPS surveys of GO and rGO, AFM image of Au/rGO, monitored peak of time-resolved PL decay profile, and nitrogen adsorption−desorption isotherms and BET surface areas of samples. This material is available free of charge via the Internet at http://pubs.acs.org/.

AUTHOR INFORMATION

Corresponding Author

*Tel: +82 52 259 2330. Fax: +82 52 259 1693. E-mail: shhahn@ulsan.ac.kr.

Author Contributions

The manuscript was written through contributions of all the authors. All authors have given approval to the final version of the manuscript.

Notes

The authors declare no competing financial interest.

ACKNOWLEDGMENTS

This research was financially supported by the Ministry of Education (MOE) and National Research Foundation of Korea (NRF) through the Human Resource Training Project for Regional Innovation (2012H1B8A2026179) and the Basic Science Research Program (2012R1A1A4A01015466).

REFERENCES

(1) Zhong, Y.; Wang, Z.; Zhang, R.; Bai, F.; Wu, H.; Haddad, R.; Fan, H. Interfacial Self-Assembly Driven Formation of Hierarchically Structured Nanocrystals with Photocatalytic Activity. *ACS Nano* **2014**, *8*, 827−833.

(2) Davíðsdóttir, S.; Petit, J. P.; Mermoux, M.; Shabadi, R.; Canulescu, S.; Almtoft, K. P.; Dirscherl, K.; Ambat, R. Interfacial Structure and Photocatalytic Activity of Magnetron Sputtered TiO_2 on

DOI: 10.1021/acsami.5b00152
ACS Appl. Mater. Interfaces 2015, 7, 3524−3531

Conducting Metal Substrates. *ACS Appl. Mater. Interfaces* **2014**, *6*, 22224−22234.
(3) Romão, J.; Barata, D.; Habibovic, P.; Mul, G.; Baltrusaitis, J. High Throughput Analysis of Photocatalytic Water Purification. *Anal. Chem.* **2014**, *86*, 7612−7617.
(4) Chen, X.; Shen, S.; Guo, L.; Mao, S. S. Semiconductor-Based Photocatalytic Hydrogen Generation. *Chem. Rev.* **2010**, *110*, 6503−6570.
(5) Devadoss, A.; Sudhagar, P.; Das, S.; Lee, S. Y.; Terashima, C.; Nakata, K.; Fujishima, A.; Choi, W.; Kang, Y. S.; Paik, U. Synergistic Metal−Metal Oxide Nanoparticles Supported Electrocatalytic Graphene for Improved Photoelectrochemical Glucose Oxidation. *ACS Appl. Mater. Interfaces* **2014**, *6*, 4864−4871.
(6) Banerjee, S.; Pillai, S. C.; Falaras, P.; O'Shea, K. E.; Byrne, J. A.; Dionysiou, D. D. New Insights into the Mechanism of Visible Light Photocatalysis. *J. Phys. Chem. Lett.* **2014**, *5*, 2543−2554.
(7) Akimov, A. V.; Neukirch, A. J.; Prezhdo, O. V. Theoretical Insights into Photoinduced Charge Transfer and Catalysis at Oxide Interfaces. *Chem. Rev.* **2013**, *113*, 4496−4565.
(8) Marschall, R. Semiconductor Composites: Strategies for Enhancing Charge Carrier Separation To Improve Photocatalytic Activity. *Adv. Funct. Mater.* **2014**, *24*, 2421−2440.
(9) Yoo, D. H.; Cuong, T. V.; Luan, V. H.; Khoa, N. T.; Kim, E. J.; Hur, S. H.; Hahn, S. H. Photocatalytic Performance of a Ag/ZnO/CCG Multidimensional Heterostructure Prepared by a Solution-Based Method. *J. Phys. Chem. C* **2012**, *116*, 7180−7184.
(10) Bian, Z.; Tachikawa, T.; Zhang, P.; Fujitsuka, M.; Majima, T. A Nanocomposite Superstructure of Metal Oxides with Effective Charge Transfer Interfaces. *Nature Commun.* **2014**, *5*, 3038.
(11) Li, P.; Wei, Z.; Wu, T.; Peng, Q.; Li, Y. Au−ZnO Hybrid Nanopyramids and Their Photocatalytic Properties. *J. Am. Chem. Soc.* **2011**, *133*, 5660−5663.
(12) Khoa, N. T.; Pyun, M. W.; Yoo, D. H.; Kim, S. W.; Leem, J. Y.; Kim, E. J.; Hahn, S. H. Photodecomposition Effects of Graphene Oxide Coated on TiO_2 Thin Film Prepared by Electron-Beam Evaporation Method. *Thin Solid Films* **2012**, *520*, 5417−5420.
(13) Hoffmann, M. R.; Martin, S. T.; Choi, W.; Bahnemann, D. W. Environmental Applications of Semiconductor Photocatalysis. *Chem. Rev.* **1995**, *95*, 69−96.
(14) Yu, Z. B.; Xie, Y. P.; Liu, G.; Lu, G. Q.; Ma, X. L.; Cheng, H. M. Self-Assembled CdS/Au/ZnO Heterostructure Induced by Surface Polar Charges for Efficient Photocatalytic Hydrogen Evolution. *J. Mater. Chem. A* **2013**, *1*, 2773−2776.
(15) Ameen, S.; Akhtar, M. S.; Song, M.; Shin, H. S. Vertically Aligned ZnO Nanorods on Hot Filament Chemical Vapor Deposition Grown Graphene Oxide Thin Film Substrate: Solar Energy Conversion. *ACS Appl. Mater. Interfaces* **2012**, *4*, 4405−4412.
(16) Liu, J.; Lu, R.; Xu, G.; Wu, J.; Thapa, P.; Moore, D. Development of A Seedless Floating Growth Process in Solution for Synthesis of Crystalline ZnO Micro/Nanowire Arrays on Graphene: Towards High-Performance Nanohybrid Ultraviolet Photodetectors. *Adv. Funct. Mater.* **2013**, *23*, 4941−4948.
(17) Wang, X.; Yin, L.; Liu, G. Light Irradiation-Assisted Synthesis of ZnO−CdS/Reduced Graphene Oxide Heterostructured Sheets for Efficient Photocatalytic H_2 Evolution. *Chem. Commun.* **2014**, *50*, 3460−3463.
(18) Weng, B.; Yang, M. Q.; Zhang, N.; Xu, Y. J. Toward The Enhanced Photoactivity and Photostability of ZnO Nanospheres via Intimate Surface Coating with Reduced Graphene Oxide. *J. Mater. Chem. A* **2014**, *2*, 9380−9389.
(19) Yang, M. Q.; Zhang, N. Y.; Pagliaro, M.; Xu, Y. J. Artificial Photosynthesis over Graphene−Semiconductor Composites. Are We Getting Better? *Chem. Soc. Rev.* **2014**, *43*, 8240−8254.
(20) Zhang, N.; Zhang, Y.; Xu, Y. J. Recent Progress on Graphene-Based Photocatalysts: Current Status and Future Perspectives. *Nanoscale* **2012**, *4*, 5792−5813.
(21) Yang, M. Q.; Xu, Y. J. Selective Photoredox Using Graphene-Based Composite Photocatalysts. *Phys. Chem. Chem. Phys.* **2013**, *15*, 19102−19118.
(22) Zhang, N.; Yang, M. Q.; Tang, Z. R.; Xu, J. Y. Toward Improving the Graphene Semiconductor Composite Photoactivity via the Addition of Metal Ions as Generic Interfacial Mediator. *ACS Nano* **2014**, *8*, 623−633.
(23) Zhang, Y.; Tang, Z. R.; Fu, X.; Xu, Y. J. TiO_2−Graphene Nanocomposites for Gas-Phase Photocatalytic Degradation of Volatile Aromatic Pollutant: Is TiO_2−Graphene Truly Different from Other TiO_2−Carbon Composite Materials? *ACS Nano* **2010**, *4*, 7303−7314.
(24) Zhang, Y.; Tang, Z. R.; Fu, X.; Xu, Y. J. Engineering the Unique 2D Mat of Graphene To Achieve Graphene−TiO_2 Nanocomposite for Photocatalytic Selective Transformation: What Advantage does Graphene Have over Its Forebear Carbon Nanotube? *ACS Nano* **2011**, *5*, 7426−7435.
(25) Zhang, Y.; Zhang, N.; Tang, Z. R.; Xu, Y. J. Graphene Transforms Wide Band Gap ZnS to a Visible Light Photocatalyst. The New Role of Graphene as a Macromolecular Photosensitizer. *ACS Nano* **2012**, *6*, 9777−9789.
(26) Zhang, N.; Zhang, Y.; Pan, X.; Yang, M. Q.; Xu, Y. J. Constructing Ternary CdS−Graphene−TiO_2 Hybrids on the Flatland of Graphene Oxide with Enhanced Visible-Light Photoactivity for Selective Transformation. *J. Phys. Chem. C* **2012**, *116*, 18023−18031.
(27) Han, C.; Yang, M. Q.; Weng, B.; Xu, Y. J. Improving The Photocatalytic Activity and Anti-Photocorrosion of Semiconductor ZnO by Coupling with Versatile Carbon. *Phys. Chem. Chem. Phys.* **2014**, *16*, 16891−16903.
(28) Luo, Q. P.; Yu, X. Y.; Lei, B. X.; Chen, H. Y.; Kuang, D. B.; Su, C. Y. Reduced Graphene Oxide-Hierarchical ZnO Hollow Sphere Composites with Enhanced Photocurrent and Photocatalytic Activity. *J. Phys. Chem. C* **2012**, *116*, 8111−8117.
(29) Khoa, N. T.; Kim, S. W.; Yoo, D. H.; Kim, E. J.; Hahn, S. H. Size-Dependent Work Function and Catalytic Performance of Gold Nanoparticles Decorated Graphene Oxide Sheets. *Appl. Catal. A: Gen.* **2014**, *469*, 159−164.
(30) Ge, L.; Jing, X.; Wang, J.; Wang, J.; Jamil, S.; Liu, Q.; Liu, F.; Zhang, M. Trisodium Citrate Assisted Synthesis of ZnO Hollow Spheres via a Facile Precipitation Route and Their Application as Gas Sensor. *J. Mater. Chem.* **2011**, *21*, 10750−10754.
(31) Janotti, A.; Van de Walle, C. G. Native Point Defects in ZnO. *Phys. Rev. B* **2007**, *76*, 165202.
(32) Chen, J.; Feng, Z.; Ying, P.; Li, M.; Han, B.; Li, C. The Visible Luminescent Characteristics of ZnO Supported on SiO_2 Powder. *Phys. Chem. Chem. Phys.* **2004**, *6*, 4473−4479.
(33) Khoa, N. T.; Kim, S. W.; Thuan, D. V.; Yoo, D. H.; Kim, E. J.; Hahn, S. H. Hydrothermally Controlled ZnO Nanosheet Self-Assembled Hollow Spheres/Hierarchical Aggregates and Their Photocatalytic Activities. *CrystEngComm* **2014**, *16*, 1344−1350.
(34) Tian, Z. R.; Voigt, J. A.; Liu, J.; Mckenzie, B.; Mcdermott, M. J.; Rodriguez, M. A.; Konishi, H.; Xu, H. Complex and Oriented ZnO Nanostructures. *Nat. Mater.* **2003**, *2*, 821−826.
(35) Atwater, H. A.; Polman, A. Plasmonics for Improved Photovoltaic Devices. *Nat. Mater.* **2010**, *9*, 205−213.
(36) Lee, J.; Shim, H. S.; Lee, M.; Song, J. K.; Lee, D. Size-Controlled Electron Transfer and Photocatalytic Activity of ZnO−Au Nanoparticle Composites. *J. Phys. Chem. Lett.* **2001**, *2*, 2840−2845.
(37) Xing, G.; Mathews, N.; Sun, S.; Lim, S. S.; Lam, Y. M.; Gratzel, M.; Mhaisalkar, S.; Sum, T. C. Long-Range Balanced Electron- and Hole-Transport Lengths in Organic−Inorganic $CH_3NH_3PbI_3$. *Science* **2013**, *342*, 344−347.
(38) Cheng, S. H.; Yeh, Y. C.; Lu, M. L.; Chen, C. W.; Chen, Y. F. Enhancement of Laser Action in ZnO Nanorods Assisted by Surface Plasmon Resonance of Reduced Graphene Oxide Nanoflakes. *Opt. Express* **2012**, *20*, 799−805.
(39) Yuan, K.; Chen, L.; Li, F.; Chen, Y. Nanostructured Hybrid ZnO@CdS Nanowalls Grown in Situ for Inverted Polymer Solar Cells. *J. Mater. Chem. C* **2014**, *2*, 1018−1027.
(40) Yadav, H. K.; Sreenivas, K.; Gupta, V. Study of Metal/ZnO Based Thin Film Ultraviolet Photodetectors: The Effect of Induced Charges on Dynamics of Photoconductivity Relaxation. *J. Appl. Phys.* **2010**, *107*, 044507.

DOI: 10.1021/acsami.5b00152
ACS Appl. Mater. Interfaces 2015, 7, 3524−3531

(41) Roy, P.; Periasamy, A. P.; Liang, C. T.; Chang, H. T. Synthesis of Graphene−ZnO−Au Nanocomposites for Efficient Photocatalytic Reduction of Nitrobenzene. *Environ. Sci. Technol.* **2013**, *47*, 6688−6695.
(42) Giovannetti, G.; Khomyakov, P. A.; Brocks, G.; Karpan, V. M.; van den Brink, J.; Kelly, P. J. Doping Graphene with Metal Contacts. *Phys. Rev. Lett.* **2008**, *101*, 026803.
(43) Lin, W. H.; Wu, J. J.; Chou, M. M. C.; Chang, Y. M.; Yoshimura, M. Charge Transfer in Au Nanoparticle−Nonpolar ZnO Photocatalysts Illustrated by Surface-Potential-Derived Three-Dimentional Band Diagram. *J. Phys. Chem. C* **2014**, *118*, 19814−19821.

DOI: 10.1021/acsami.5b00152
ACS Appl. Mater. Interfaces 2015, 7, 3524−3531